Electric Circuit Representation of the Human Circulatory System to Estimate the Position of Nanosensors in Vessels

Jorge Torres Gómez[a], Jorge Luis González Rios[b], Falko Dressler[a]

[a]*School of Electrical Engineering and Computer Science, TU Berlin, Germany*
[b]*SnT, University of Luxembourg, Luxembourg*

Abstract

Nanodevices are the focus of research enhancing the detection and treatment of diseases in the human body. Focusing on the scenario where nanosensors are flowing with the blood in the human circulatory system (HCS), in this work, we investigate a model to predict their distribution along the various vessel segments. Although various approaches report solutions for localizing nanosensors in the body, it is also relevant to derive their stationary distribution along the vessel segments as a prior step to assess their actuation and sensing capabilities in the body. We use a Markov chain formulation to derive the stationary distribution of nanosensors. We evaluate the transition probabilities relying on the representation of vessels with electric circuit components. We implement the electric circuit representation of the left ventricle in the heart and the arteries to find the blood flow at vessel bifurcations and then compute the Markov chain probabilities. Our system also allows to reveal the dynamics of the movement of nanosensors during human activity. We illustrate results in two regimes as low and high activity to mimic the case when being at rest or doing sports.

Keywords: Human Circulatory System, Electric Circuit Simulator, Localization, Blood Pressure, Nanosensors, Nanosensor Flow

1. Introduction

Research on precision medicine solutions is, among others, focusing on nanotechnology [1]. Nanosensors are assumed to detect small concentrations of biomarkers and trigger alerts in the early stages of potential diseases. A key to success is the ability to predict nanosensor locations due to their limited technical sensing capabilities.

In this work, we estimate the concentration level of nanosensors along the various body regions when they are moving within the blood flow. Blood vessels provide a network where flowing nanosensors may passively reach various body regions and detect abnormalities, e.g., cancer cells [2, 3, 4]. Yet, estimating the total number of nanosensors along the various vessel segments is a challenging endeavor due to the random paths each individual nanosensor takes.

Driven by the blood flow, the exact location of nanosensors in vessels remains a challenging problem due to the non-predictable paths through arteries, capillaries, and veins. Jumps at bifurcations occur randomly, resulting in a random process of the path trajectory of nanosensors in the vessels. Recent research addresses this issue through the use of anchor nodes and the exchange of a reference coordinate location using wireless technology [5, 6], or calculating the distance to reference anchor nodes through hop-count metrics in the received messages [7, 8]. In a different approach, machine learning (ML) methods have been applied to leverage the traveling time of the nanosensor as an indicator of the path circuit in the body [9].

Despite the various approaches for self-localizing nodes in the body, it is also relevant to derive their stationary distribution while flowing in the human circulatory system (HCS). The stationary distribution will provide the concentration level of nanosensors along the vessel segments. Estimating this distribution becomes critical later to assess their clustering formation capabilities, ultimately defining their sensing and actuating performance. Due to the limited resources of individual nanosensors, they must actuate in clusters to enhance sensing and actuation capabilities [10].

In this work, we follow our previous methodology in [11, 12], where the HCS is modeled through a Markov chain, and its transition matrix is evaluated relying on the electric circuit representation of the vessels. For the electric circuit, we reuse the complete design for the arteries by Noordergraaf et al. [13], which accurately represent the main arteries for a standard person of height 1.75 m and weight of 75 kg (see [14]). Extending this solution, in this paper, we include an electric circuit component for the left ventricle replicating the blood pressure produced by the heart at the mitral valve. The design for the left ventricle follows the work by Rideout [15], where the pressure and blood flow match close to standard physiological parameters. The mixed synthesis of both circuits, for the heart

Email addresses: torres-gomez@ccs-labs.org (Jorge Torres Gómez), jorge.gonzalez@uni.lu (Jorge Luis González Rios), dressler@ccs-labs.org (Falko Dressler)

Article published in Elsevier Nano Communication Networks 40 (2024) 100499. (10.1016/j.nancom.2024.100499)

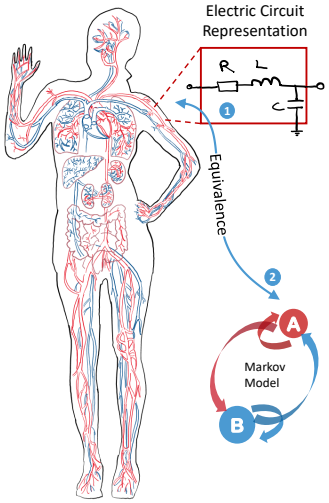

Figure 1: Electric-circuit representation in the arteries.

and the arteries, allows for flexibly simulating the pressure and flow with the heart rate.

Using the electric circuit design, we evaluate the stationary distribution of nanosensors applying the two-step model in Fig. 1. In the first step, the flow in the vessel segments is computed directly from the currents in the electric circuit. In the second step, the transition probabilities of the Markov chain are computed based on the ratios of these flows. In this way, the Markov model results equivalent to the electric circuit to estimate the position of the nanosensor with time. Based on the Markov chain representation, it is then possible to predict the stationary distribution of nanosensors along the vessels.

Using the methodology in Fig. 1, we can also asses particular individuals whenever the electric circuit parameters are properly tuned. Although the electric circuit design we use from Noordergraaf et al. [13] refers to a prototype individual, the circuit can be re-synthetized with the vessel's physiological parameters such as the radius, thickness, and length. With such a design, this methodology finds applicability to assess the nanosensor capabilities to detect and actuate on targets in particular individuals.

The main contributions of our paper can be summarized as follows:

- We implement a more complete representation of the HCS merging the electric design for the veins in [13] with the electric circuit for the left ventricle as in [15]. Including the design for the heart allows for illustration of the impact of human activity in the nanosensor distribution, i.e., low or high activity regimes.
- We characterize the HCS in the frequency domain, allowing us to visualize the dependency of the blood pressure with the heart frequency and along various vessel segments. Such a dependency allows also visualizing frequency ranges where the flow of nanosensors is favored.
- We derive results for the stationary distribution of nanosensors in the vessels with the activity. Specifically, we illustrate results when the person is at rest or in a very active regime, like doing sport.

The rest of our paper is structured as follows. Section 2 discusses relevant research on localizing nanosensors and the use of electric-circuit designs with Markov models to estimate their distribution along the vessel segments. Section 3 introduces the electric circuit implementation for the heart and the arteries. We also illustrate partial results accounting for the pressure and flows with the heart rate. Section 4 provides the theoretical framework to evaluate the stationary distribution of nanosensors with the blood flow as reported by the electric circuit design. Section 5 illustrates the results of applying the Markov model for transition probabilities, nanosensor pathways, and location. Finally, Section 6 concludes the paper.

2. Related Work

Various papers address the localization of nanosensors inside the human body based on a coordinate reference system. Coordinates in the nano-scale often rely on proximity-based or geometrical approaches [16]. In the proximity-based approach, reference coordinates are, for example, provided by near-field inductive coupling mechanism [17] or graphene-based technologies between anchor nodes (located in the surface of the skin) and the flowing nanosensors [6]. Nanosensors getting their coordinates from anchor nodes become virtual reference nodes for other nodes navigating deeper inside the body.

Geometrical approaches perform localization upon signal features like received signal strength (RSS), angle of arrival (AoA), and time of flight (ToF) [16], or using a hop counting mechanism [18, 19]. Considering the limited computational capabilities of nanosensors, Lemic et al. [16] proposes using the two-way ToF, avoiding implementing synchronization mechanisms. The ToF is computed based on the time stamps of the transmitted and reflected signals from a destination node. Furthermore, Wake-up Radio (WuR)-based solutions are included to save the limited energy capacities of nanosensors [5]. Zhou et al. [7] propose to localize sensors by estimating the distance using the RSS, i.e., the amplitude of the received signal.

Using the hop count mechanisms, nodes evaluate their distance to known-location reference nodes by counting the number of hops a packet traveled before reception [19]. Non-anchor nodes increase the hop count of packets (integer value) upon reception before retransmission. Further enhancing localization capabilities, Stelzner and Traupe [18] suggest to include three gateways for three independent hop counts, located in the two shoulders and in one of the two hips.

In a different approach, in our previous work, we researched the stationary distribution of nanosensors in the human body [11, 20]. Due to the regular flow of blood, the

amount of nanosensors per vessel segment is expected to remain constant, irrespective of the individual nanosensor's location. We derive such distribution when modeling the flow of nanosensors with a Markov chain [11]. The transition matrix is obtained using the Markov chain circuit representation. Based on this representation, we interpret the parameters of the circuit representation with the blood flow at vessels' bifurcations and use the electric circuit representation of the HCS to obtain the corresponding values of flows [20].

The electric circuit representation of the human vessels is conceived as 0-D models [21, 22, 13], providing the average flow and pressure (over the geometric coordinates of vessels), while significantly reducing computational resources. The variable time evolution of pressure and flow per vessel segment is readily given as voltages and currents. Electric components and physiological parameters are interrelated as the resistor to model the resistance produced by the blood viscosity, capacitors to the compliance of vessels, and inductors to the inertia of the blood.

In the literature, reported electric models for the HCS focus on the heart. When modeling the heart, the systemic circulation is simplified to only one network. When modeling the arteries, they are implemented as a cascade connection of L and Π two-ports networks [22, 23, 13]. Since early work by Snyder and Rideout [24], Rideout [15], only a few works tried modeling the HCS as a complete connection of arteries, capillaries, and veins. The work in [15] provides a complete representation of the HCS, but the model lacks to implement the arms. The legs are analyzed as a single network, thereby providing fewer details.

In this work, we extend our previous contribution in [12] including an electric circuit model for the heart. For the first time, the electric circuit allows adjusting the heart frequency and modeling different activities flexibly. For instance, when the body is at rest with lower frequency rates, or when practicing sports with higher rates. The complete design results from integrating the arteries model from [13] with the heart model from [15].

3. Electric Circuit Design for Heart and Arteries

The electric circuit implementation consists of two parts: the left ventricle of the heart and the arteries, arterioles, and capillaries. We integrate both circuits using the heart design as a stimulus for the arterial design. In the following, we provide details on their synthesis, analysis, and integration between the two circuits. The circuit is realized in Simulink/Matlab® using resistors, inductors, capacitors, and diodes from the Simscape library. We made the complete design publicly available, which provides the pressure and blood flow along the various vessel segments. [1]

3.1. Electric circuit design for the heart

The electric circuit design for the left ventricle in the heart follows the scheme in Fig. 2 as described in [15, Fig. 4.2.1 pag. 79]. The model integrates the left ventricle and the systemic circulation comprising all the arteries, capillaries, and veins as a T-topology (R_{SA}, C_{CA}, and R_{CA}). It operates with two fixed voltage sources representing the atrial and the central venous pressures, P_{AT} and P_{SV}, respectively.

As for the left ventricle, the variable capacitor C recreates the diastole and systole periods in the heart. During systole, the capacitor has the highest capacitance – under the highest flexibility of muscles and blood volume in the ventricle (as it fills-in with oxygenated blood from the lungs). Diastole is modeled with the lowest capacitor value – this is when blood is pumped out to the arteries, and the ventricle volume becomes lower. The variable capacitance is implemented with a clipped sine wave of amplitude $\frac{1}{S_{\mathrm{LD}}}$ for the diastole, and a constant value for the systole as $\frac{1}{S_{\mathrm{LS}}}$. The two diodes, MV and AV, model the opening and closing of the mitral and ventricle valves, respectively.

The circuit provides the ventricular pressure and volume as depicted in Fig. 2 a) and uses the parameters given in Table 1 in centimetre–gram–second system (CGS) units. With a heart period of 75 beats/min, the amplitude of peaks results in 105 mm Hg during systole, while the volume of the ventricle raises from 50 mL to 130 mL during diastole. These resulting values are standard hemodynamic parameters for the left ventricle in the heart (see [25, Fig. 9.8 pag. 118]). Besides, the cardiac cycle in Fig. 2 b) depicts the standard counter-clockwise loop dependency between the ventricular pressure and the volume. With low pressure, the volumes rise due to the fill-in of blood when the mitral valve opens during diastole. The process happens until the volume starts decreasing again and the ventricular pressure increases to pump blood to the arteries when the arterial valve is open.

Furthermore, this circuit allows the flexible generation of ventricle pressures for various cardiac activities. For the purpose of illustration, we depict in Fig. 3 the frequency heart range of a male individual of height 1.68 m, 38 years old, and weight of 81 kg. These readings were conducted with the Samsung Health app for eleven months. For this specific individual, the heart frequency can be around 75 beats/min in a low activity regime (when being at rest); however, for a very active regime (when doing sports), the heart frequency increases above the 150 beats/min. These activities can be emulated when directly tuning the frequency heart in the circuit design with the capacitor value. This circuit introduces the flexibility to model different regime activities to evaluate pressure and flows along the vessel segments. [2]

[1] The design for the electric circuit representation of the HCS is accessible in https://www.mathworks.com/matlabcentral/fileexchange/109935-electric-circuit-representation-of-the-human-arteries

[2] Although we do not discuss here, we also remark that the electric circuit model can also be used to flexibly model the variability for other physiological parameters like vessel dilation, for instance. The

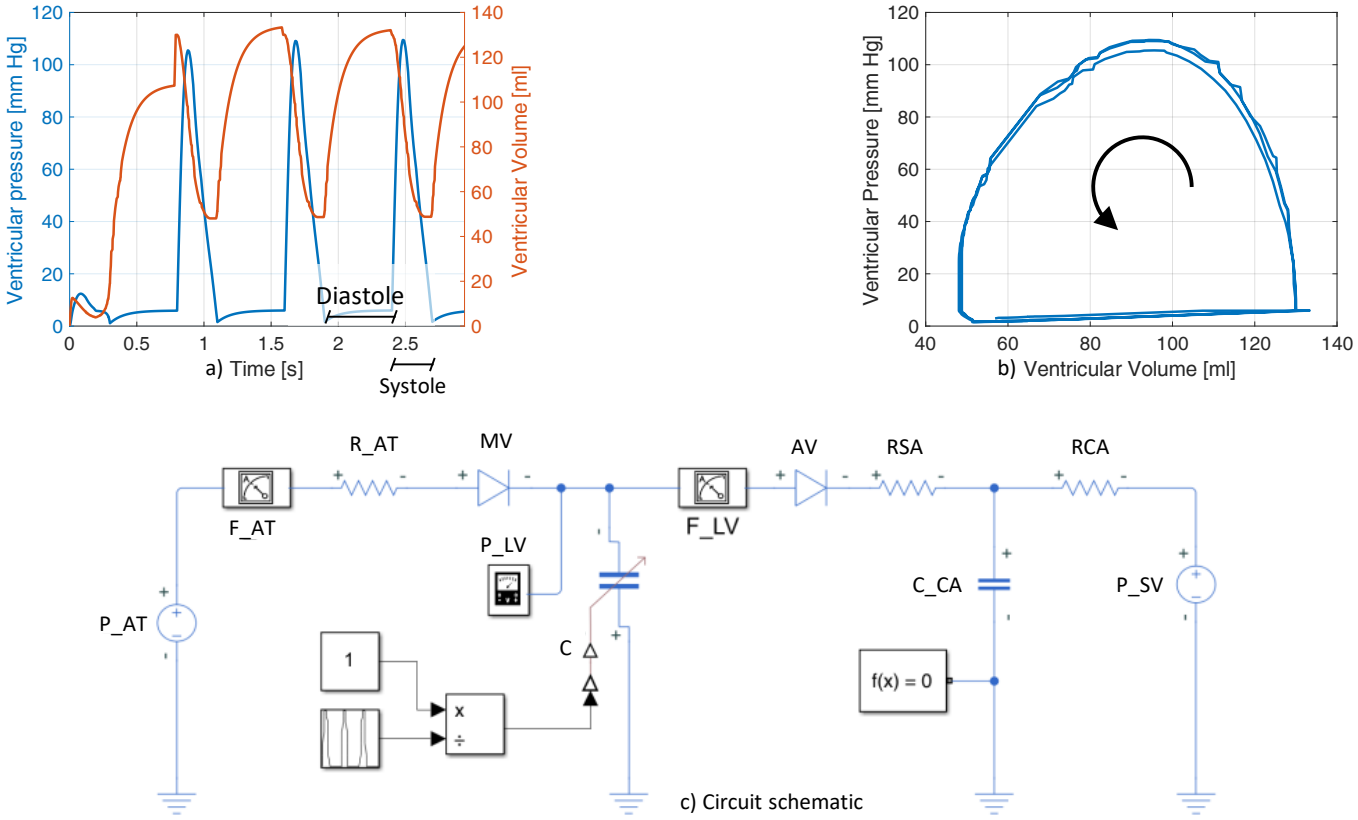

Figure 2: Electric circuit for the heart [15] and output blood flow, pressure and cardiac cycle in the left ventricle.

	Parameter	Variable	Value
Hemodynamic	Diastole stiffness	S_{LD}	$75\,\text{gm/cm}^2/\text{s}^2$
	Systole stiffness	S_{LS}	$2500\,\text{gm/cm}^2/\text{s}^2$
	Atrial Pressure	P_{AT}	6 mm Hg
	Venous Pressure	P_{SV}	3 mm Hg
	Diastolic period	T_{D}	0.5 s
	Systolic period	T_{S}	0.3 s
	Heart rate	f_{heart}	75 beats/min
Electric	Mitral valve resistance	R_{AT}	$8\,\text{g/cm}^4/\text{sec}$
	Aorta impedance	R_{SA}	$200\,\text{g/cm}^4/\text{sec}$
	Sistemic circulation resistance	R_{CA}	$1250\,\text{g/cm}^4/\text{sec}$
	Sistemic circulation compliance	C_{CA}	$0.0022\,\text{cm}^4\text{sec}^2/\text{g}$

Table 1: Parameters of the electric circuit model for the heart [15]. Units are given in the CGS system, where the values of resistances and capacitors are related to g, cm, and sec.

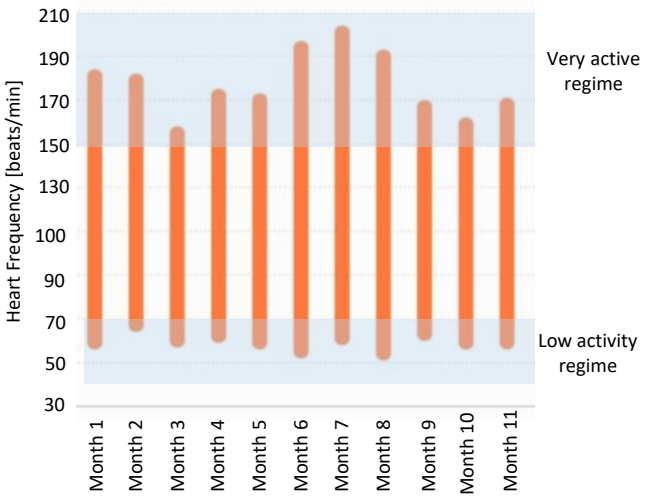

Figure 3: Illustration of the frequency rate, along eleventh months, for one specific male individual of height 1.68 m and 81 kg. The plot exhibits two different regimes: low activity regime where $35\,\text{beats/min} < f_{\text{heart}} < 70\,\text{beats/min}$, and very active regime (doing sport) where $150\,\text{beats/min} < f_{\text{heart}} < 210\,\text{beats/min}$.

3.2. Electric circuit design for the arteries

We implement the electric circuit for the major arteries following the design provided by Noordergraaf et al. [13]. Fig. 4 illustrates the connection of blocks in the center

value of the resistors, to model the vessel radius, and capacitors for their elasticity, can be parameterized as a function of other variables like the body temperature to later model the impact on the blood flow and pressure.

body where each aorta segment is implemented with the cascade connection of blocks denoted as `RLC_x`. Each block comprises an L-inverted topology, consisting of the series connection of a resistor and an inductor, with the shunt connection of a capacitor. The resistor, inductor, and capacitor simulate the resistance to the blood flow, the blood's inertia, and the vessel's compliance, respectively, according to the specific segment in the aorta. Given a vessel segment of length Δl, radius R_v, and vessel thickness h, the electric circuit components can be computed as [15]

$$R = \frac{8\pi\mu\Delta l}{\pi R_v^2}, L = \frac{9\rho\Delta l}{4\pi R_v^2}, C = \frac{3\pi R_v^3 \Delta l}{2Eh}, \tag{1}$$

where μ is the blood viscosity, ρ is the blood density, and E is the Young's bulk modulus of elasticity.

We also include diodes to guide the flow from arteries to the next segments in the same way the blood flows in the vessels. Due to the reactance of the capacitors and inductors, a flow back may be experienced due to the stored energy in these circuits. In total, we implemented 128 blocks to complete the representation of the arteries in the head, center body, arms, and legs.

Finally, to reproduce the signal from the heart, we integrate this circuit to the scheme derived by Rideout [15] (see Fig. 2), avoiding introducing loads. We combine the two designs in the same canvas using the ventricle pressure as an independent voltage source with the circuit of Noordergraaf et al. [13].

3.3. Analysis and validation of the electric circuit design

We analyze the circuit behavior in the frequency domain, obtaining the transfer function per block. The transfer function for each block is directly given as

$$H_i(s) = \frac{\frac{1}{sC_i}||Z_{\mathrm{L},i}}{R_i + L_i s + \frac{1}{sC_i}||Z_{\mathrm{L},i}}, \tag{2}$$

in the complex frequency (s) domain [26]. This transfer function includes not only the circuit elements of the given vessel segments (as R_i, L_i, C_i), but also the loading effect from the next blocks, here denoted as $Z_{\mathrm{L},i}$. As depicted in Fig. 5, the load impedance will be in parallel to the shunt capacitor at block i, denoted as the $||$ operator. Besides, the load encompasses one of the following arrangements (cf. Fig. 4):

i) a termination resistance (e.g., R_64);
ii) the input impedance of a single circuit block k, $Z_{\mathrm{in},k}$, modeling a different vessel segment; or
iii) the equivalent impedance of the parallel connection of several blocks $k_1, \ldots, k_n$, i.e., $Z_{\mathrm{in},k,1}|| \ldots ||Z_{\mathrm{in},k,n}$.

where Z_L is determined using the same procedure as in [20]. To compute the load impedance, we represent each block through its transmission matrix $\mathbb{T}_i$ as [27]

$$\mathbb{T}_i = \begin{bmatrix} 1 - \omega^2 C_i L_i + j\omega C_i R_i & R_i + j\omega L_i \\ j\omega C_i & 1 \end{bmatrix}, \tag{3}$$

from which we can obtain the input impedance as [28]

$$Z_{\mathrm{in},i} = \frac{\mathbb{T}_i(1,2) + \mathbb{T}_i(1,2)\, Z_{\mathrm{L},i}}{\mathbb{T}_i(2,2) + \mathbb{T}_i(2,1)\, Z_{\mathrm{L},i}} \tag{4}$$

where $\omega = 2\pi f$ is the angular frequency, f is the linear frequency, and j is the imaginary unit.

Using the relation in Eq. (4), we can recursively compute the output impedance for each block as it is equal to the input impedance of the next one, i.e., $Z_{\mathrm{L},i} = Z_{\mathrm{in},i-1}$. Starting at the terminator resistances, the input impedance from each block is computed iteratively. To illustrate, Fig. 6 depicts the frequency response amplitude for vessel segments corresponding to head, hands, and feet in the heart frequency range $30 - 220$ beats/min. We also highlight regions where the person is at a low or high activity regime. We compute the frequency response after multiplying those from individual blocks along the path. As expected, the circuit increases the frequency response amplitude in the high-activity regime, thereby increasing the perceived pressure at the head, hands, and feet. Besides, the circuit exhibits a local maximum in the sport region in favor of a better flow to the different tissues.

Figures 7 and 8 provide the resulting pressure in the arms and the legs, those directly derived from the connected voltage meter when $f_{\mathrm{heart}} = 75$ beats/min. In accordance with the blood pressure behavior at different vessel segments, see [25, Fig. 14-2 pag. 172], the most considerable oscillation is derived in the left ventricle (heart), and its elongation is reduced in the arteries of the arms and legs. We also remark on the increased amplitude in the large arteries (e.g., Aorta Carotis) compared to the left ventricle as typical behavior of the blood pressure in vessels.

We remark that the amplitude of pressure in the left ventricle is higher than reported in Fig. 7. The lower amplitude is due to the simulation sampling time we used to speed up the simulator (10^{-2} in this case). The amplitude can be updated when reducing this time or increasing the atrial pressure (voltage source $P_{\mathbf{AT}}$).

4. Markov Model Representation of HCS

The path trajectory of the flowing nanosensors in the human circulatory system can be modeled as a transition between stages, defined in one-to-one correspondence with the vessel segments. Assuming that transitions at bifurcations (to the next vessel segment in the arteries) happen randomly and independent of the previously visited vessel, the traveling path of the nanosensor can be modeled using a Markov chain approach [29].

Fig. 9 depicts the conceived stages for the Markov model following the variety of artery segments represented by the electric circuit design in Section 3. The veins in the Markov model are included when mirroring the corresponding artery (due to the symmetry of the human body), except for the head where the veins are reduced to two out of four, just for the sake of simplicity. In total, 51 stages represent

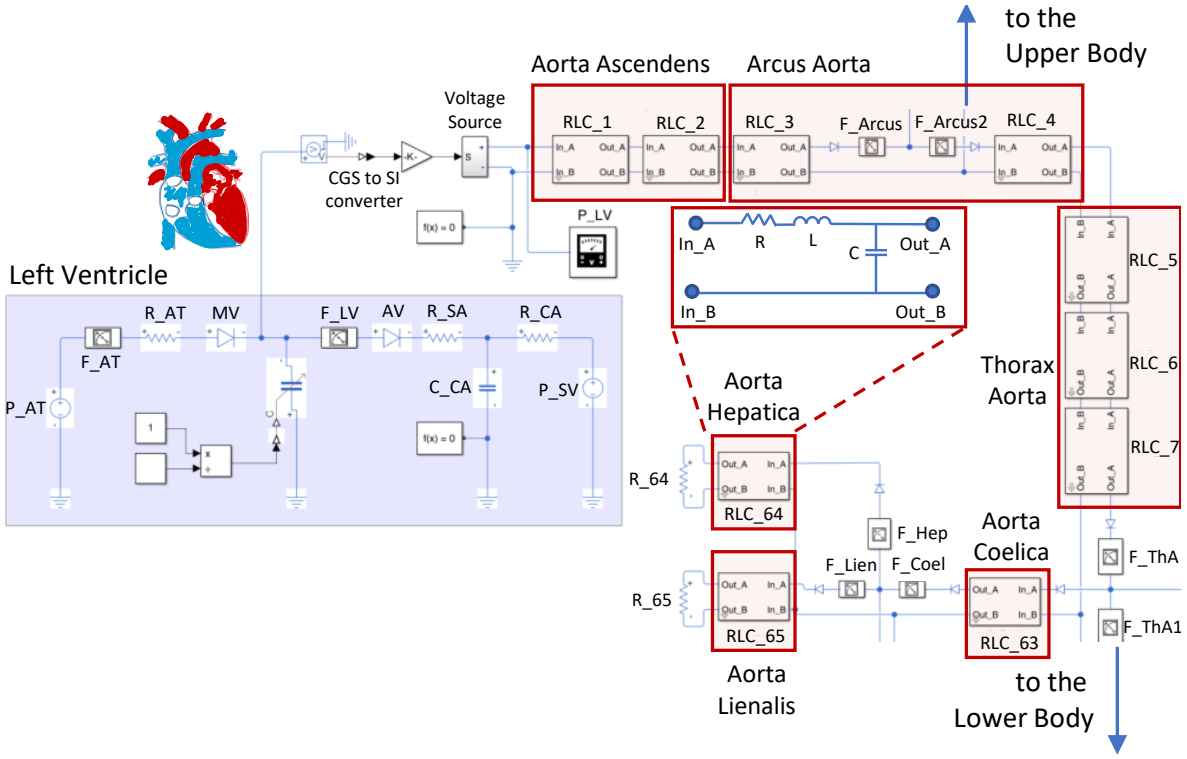

Figure 4: Electric circuit design of the human arteries following the design by Noordergraaf et al. [13].

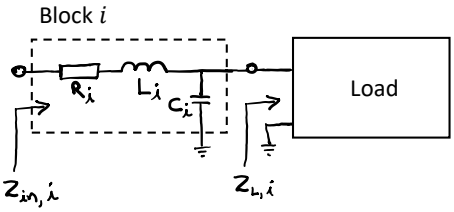

Figure 5: Output interface in the circuit diagram.

arteries, capillaries, and veins, as listed in Table 2. In contrast to our previous design in [11, Fig. 5], the current one introduces additional stages accounting for the two arms and the two legs. A more complete representation is provided here due to the available model of our circuit design.

The Markov model is completely defined by its transition matrix, denoted as $\Pi = \{p_{i,j}\}$, where $p_{i,j}$ are the transition probabilities. Besides, the stationary distribution of nanosensors can be directly evaluated when solving for $\boldsymbol{\nu}$ in

$$\boldsymbol{\nu} = \boldsymbol{\nu}\Pi. \tag{5}$$

That is, the probability of finding a nanosensor s on a given vessel segment k can be directly computed from the components of the vector $\boldsymbol{\nu}$ as

$$P_{s,k} = \nu_k, \tag{6}$$

based on which we can estimate the concentration of nanosensors on a given vessel segment as $P_{s,k} \times N_s$, where N_s are the total of nanosensors flowing in the HCS.

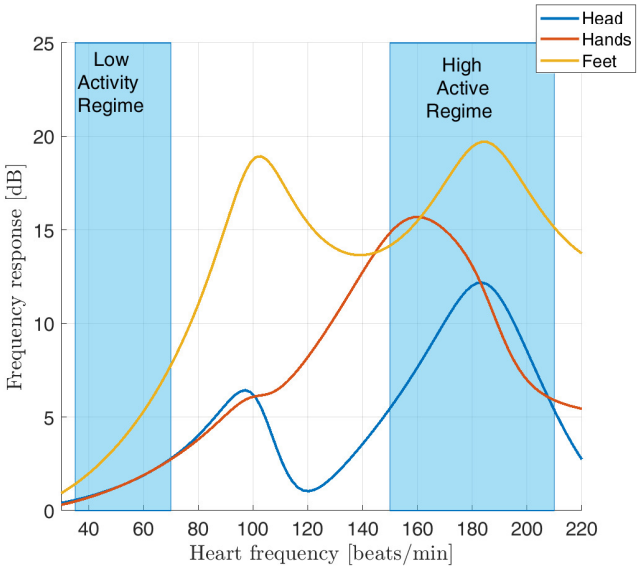

Figure 6: Frequency response for different activities, when resting ($35\,\text{beats/min} < f_{\text{heart}} < 70\,\text{beats/min}$) and when doing sports ($150\,\text{beats/min} < f_{\text{heart}} < 210\,\text{beats/min}$).

The relation in Eq. (6) will ultimately depend on the transition probabilities between states of the Markov model. To compute those, we rely on the equivalent circuit representation of the Markov model comprised of nodes and oriented loops [30]. To illustrate, Fig. 10 depicts on the left side the representation of a Markov chain composed of 6 stages. The right side depicts its equivalent representation with three oriented loops. For the equivalent representa-

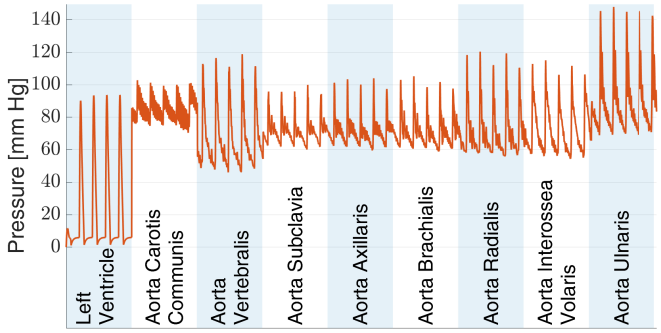

Figure 7: Blood pressure in head and arms for $f_{\text{heart}} = 75\,\text{beats/min}$.

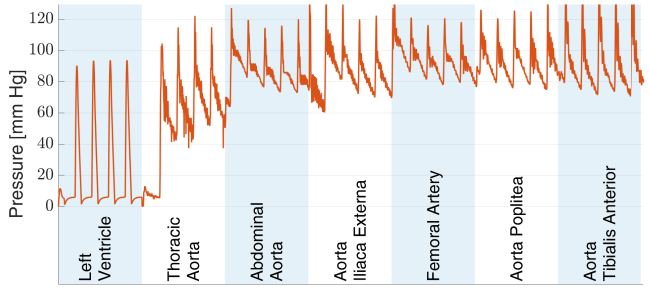

Figure 8: Blood pressure in legs for $f_{\text{heart}} = 75\,\text{beats/min}$.

tion, each stage in the Markov model must be connected with at least one loop in the circuit model.

In the circuit representation, the oriented loops represent those closed paths in the Markov model where a particle might travel. For instance, based on the representation in Fig. 10 left, we can define three independent, oriented loops, all of them intercepting through the nodes s_1, s_2, and s_3, as represented in the right side of the figure. The remaining nodes are connected to s_1, s_2, and s_3 in their corresponding loops with the weights ω_1, ω_2, and ω_3. According to [30], this equivalent representation is given by the unique relation between the weighted coefficients (ω_1, ω_2, and ω_3) along with the loops and the transition probabilities ($p_{i,j}$) in the Markov model.

The relation between the transition probabilities $p_{i,j}$ and coefficients ω_j is found as a ratio between the sum of coefficients connecting the nodes i and j and the sum of coefficients for all loops that pass through the node i, see [30]. For instance, if we want to evaluate the transition probability $p_{1,3}$ with these coefficients, it yields

$$p_{1,3} = \frac{\omega_1}{\omega_1 + \omega_2 + \omega_3}, \tag{7}$$

as the ratio between the coefficient corresponding to the loop where the destination s_3 is located (ω_1 in this case), and the sum of the coefficients concerning the loops intercepting the departing stage s_1 (in this case three loops).

The way these coefficients are sketched (constant along the loop), together with the circuit topology of this representation, let us interpret this coefficient as mesh currents

Markov States	Vessel Segment
S1	Right Heart
S2	Lungs
S3	Left Heart
S4	A. Ascendens
S5	Arcus Aorta
S6	A. Anonyma
S7	Head
S8 (S17)	A. Subclavia s. (d)
S9 (S18)	A. Axillaris s. (d.)
S10 (S19)	A.Brachialis s. (d.)
S11 (S20)	A. Radialis s. (d.)
S12 (S21)	A. Interossea Volaris s. (d.)
S13 (S22)	A. Ulnaris s. (d.)
S14 (S23)	V. Brachialis s. (d.)
S15 (S24)	V. Axillaris s. (d.)
S16 (S25)	V. Subclavia s. (d.)
S26 (S27)	Jugular Vein s. (d.)
S28	Superior Vena Cava
S29	Thoratica Aorta
S30	Thorax and Back
S31	Abdominal Aorta
S32	Mesenterica Superior
S33	Mesenterica Inferior
S34	Liver
S35	Kidneys
S36	Abdominal Vein
S37	Inferior Vena Cava
S38 (S45)	A. Iliaca Communis and Externa s. (d.)
S39 (S46)	A. Femoralis Profundis s. (d.)
S40 (47)	A. Poplitea s. (d.)
S41 (S48)	A. Tibialis Anterior s. (d.)
S42 (S49)	A. Tibialis Posterior s. (d.)
S43 (S50)	V. Poplitea s. (d.)
S44 (S51)	V. Iliaca Communis and Externa s. (d.)

Table 2: Association between stages and vessel segments.

from the electric circuit that simulate the same HCS as the Markov model does [11]. That is, mesh currents are also constant along closed-loops [27], and they superpose in the same way the coefficient does in the circuit representation of the Markov model. In this way, the transition probability in Eq. (7) can be computed considering the mesh currents in the electric circuit representation as

$$p_{1,3} = \frac{I_1}{I_1 + I_2 + I_3}, \tag{8}$$

when interpreting the coefficients as mesh currents (I_k). Looking closer to Eq. (8), this evaluation also yields the

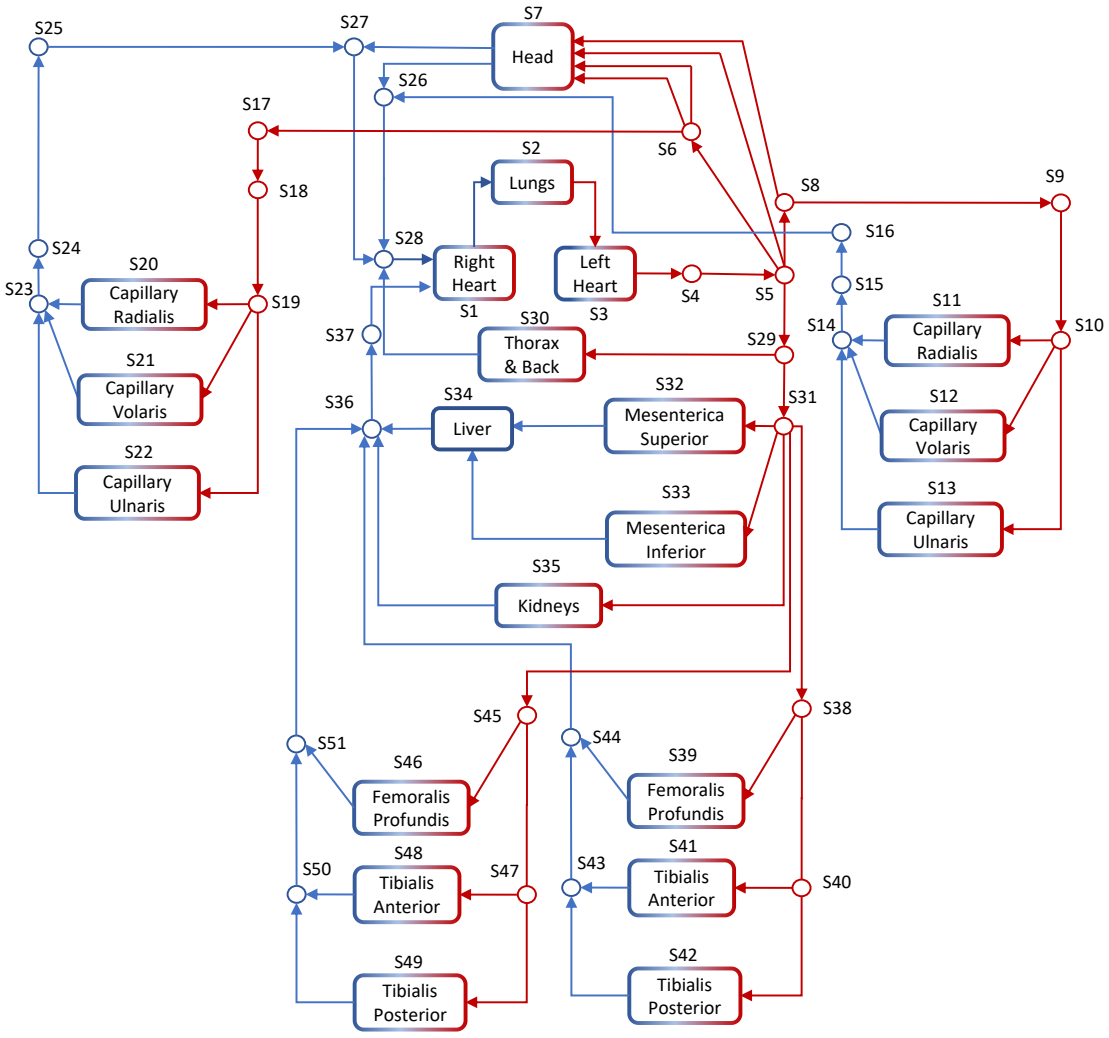

Figure 9: Markov model representation of the human circulatory system.

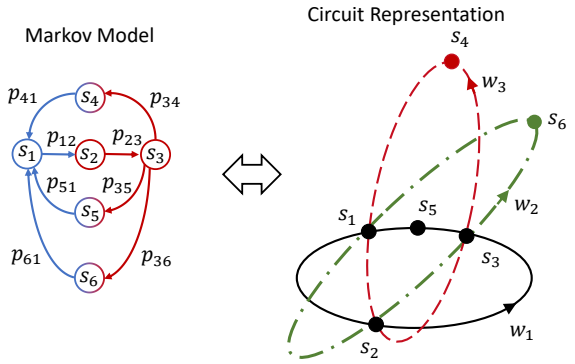

Figure 10: Circuit representation of a Markov chain.

ratio of the total of particles traveling to the node S_3 and the sum of all particles at S_1. This evaluation agrees with the intuitive evaluation of the transition probability (Fermat's definition) as the ratio between the total of successful events (particles traveling to S_3) and the total of events (total of particles at S_1).

Extending this analysis to the original Markov model in Fig. 9, the transition probability from Arcus Aorta to Aorta Thoratica can be computed as the ratio of the output current from s_5 to s_{29}, to the input current to s_5, for instance. The same applies to the other bifurcations as well. Intuitively, this also matches the definition of probability as a ratio of successful events to total events. Looking at the corresponding ratio of flows as the total of particles moving to one branch compared to the total of particles at the bifurcation, let to interpret it as a metric of probability.

In this way, the electric circuit for the arteries in Section 3 lets us compute the Markov model's transition probabilities at the bifurcations. Besides, because transitions in the veins happen with a probability equal to 1, then the corresponding transition matrix of the Markov model can also be fully determined [3]. According to this methodology,

[3]We remark that according to the model in Fig. 9, there are two output veins represented in the head towards the stages S26 and S27. For the sake of simplicity, here we assume equal probability. However, a more accurate model can be obtained according to the ratio of flows from both veins (in this case Carotid and Vertebralis).

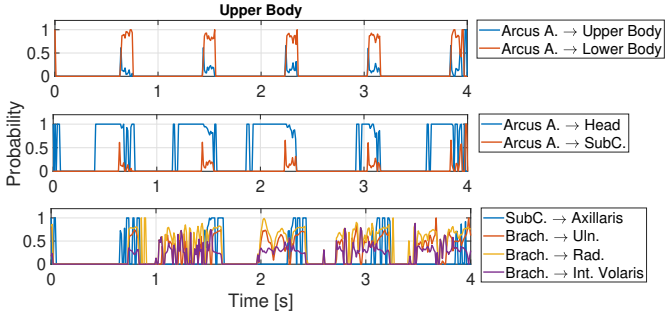

Figure 11: Transition probabilities in the upper body for $f_{\text{heart}} = 75\,\text{beats/min}$.

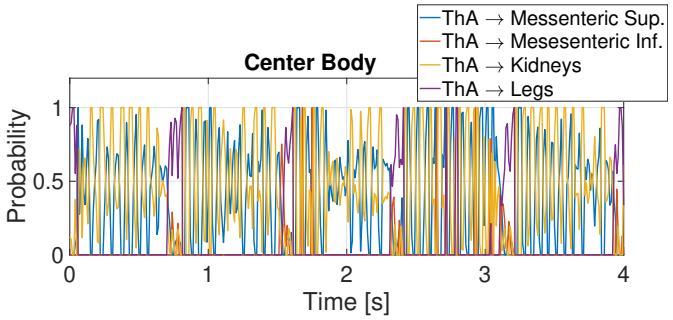

Figure 12: Transition probabilities in the center body for $f_{\text{heart}} = 75\,\text{beats/min}$.

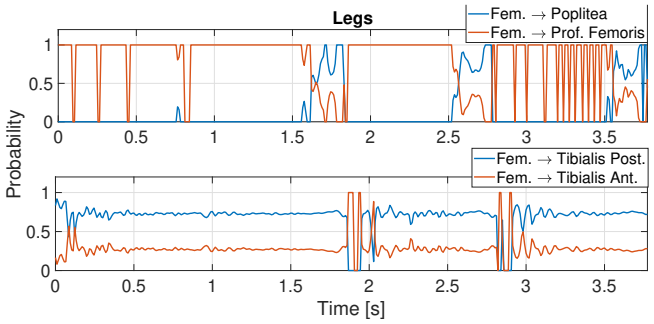

Figure 13: Transition probabilities in the lower body for $f_{\text{heart}} = 75\,\text{beats/min}$.

the Markov model and the electric circuit will be equivalent to determining the nanosensor's position with time. The nanosensor's position can be solved in the electric circuit model with its initial position and the guiding flow along the various vessel segments. With the Markov chain, the nanosensor's position will be fully described with the corresponding probabilistic model and evaluate the transition probabilities with the electric circuit model.

5. Results

We use the circuit in Section 3 to evaluate the transition probabilities of the Markov model. Similarly to Eq. (8), we derive the currents per loop and evaluate the corresponding ratios to compute the transition probabilities. We illustrate results concerning the transition matrix for the Markov model and its use to predict the concentration level of nanosensors along the vessels. We also comparatively illustrate results with the change of activity, being at rest when $f_{\text{heart}} = 75\,\text{beats/min}$ and doing sport when $f_{\text{heart}} = 170\,\text{beats/min}$.

5.1. Transition probabilities

Figures 11 to 13 show the transition probabilities with time at main bifurcations in the upper, center, and lower bodies. We compute the transition probabilities directly evaluating the ratio of corresponding current flows, as described in Eq. (8), where the flow is measured by current meters located in the design (e.g., the blocks `F_ThA` and `F_ThA1` in Fig. 4) and $f_{\text{heart}} = 75\,\text{beats/min}$.

As shown in Fig. 11, transitions are mostly favored in the direction of the lower body than the upper body. That is, from the left ventricle (S4) a larger flow follows to the lower body through the Arcus Aorta (S5), which is in correspondence to the larger cross-sectional area of the Thorax Aorta (S31). This result also matches our previous calculation of transition probabilities in [11, Fig. 7] using the electric circuit design from [24, 15], where the larger probability is also in the direction of the lower body. Besides, according to the plots in Fig. 11, most of the time nanosensors will travel to the head (through Carotis and Vertebralis) rather than to the arms in the direction of the Subclavia and the Aorta Axillaris.

In the center body (cf. Fig. 12), most of the time, transitions happen to the kidneys and to the Mesenterica Superior. Fewer transitions happen to the Mesenterica Inferior or the legs with time. Besides, accounting for the lower body (cf. Fig. 13), we remark the less variability of the transition probabilities with time in the legs when compared to the upper and lower bodies. This results from less pressure variability as these body regions are more distant from the heart. According to these plots, most of the time nanosensors will travel through the Profundis Femoris in the legs rather than to the Poplitea or the Posterior and Anterior Tibialis.

5.2. Distribution of nanosensors in the body

Using the above transition probabilities at the bifurcations, we complete the transition matrix of the Markov model. We average these transition probabilities over time and set them equal to one for the transition in the veins. In the case of the output veins from the head, we assume an equal probability to travel through the Vertebralis or the Carotis for the sake of simplicity. However, more accurate values can be derived based on the flows on each vessel.

Fig. 14 illustrates the obtained transition probabilities for $f_{\text{heart}} = 75\,\text{beats/min}$. To highlight the most probable transitions, the width of the arrows signifies where the averaged transition probabilities are one, higher, or less than 0.5. As this graph shows, the larger transition probabilities are obtained at bifurcations to the head, the Mesenterica superior in the center body, the Femoris Profundis, and the Tibialis Posterior in the legs.

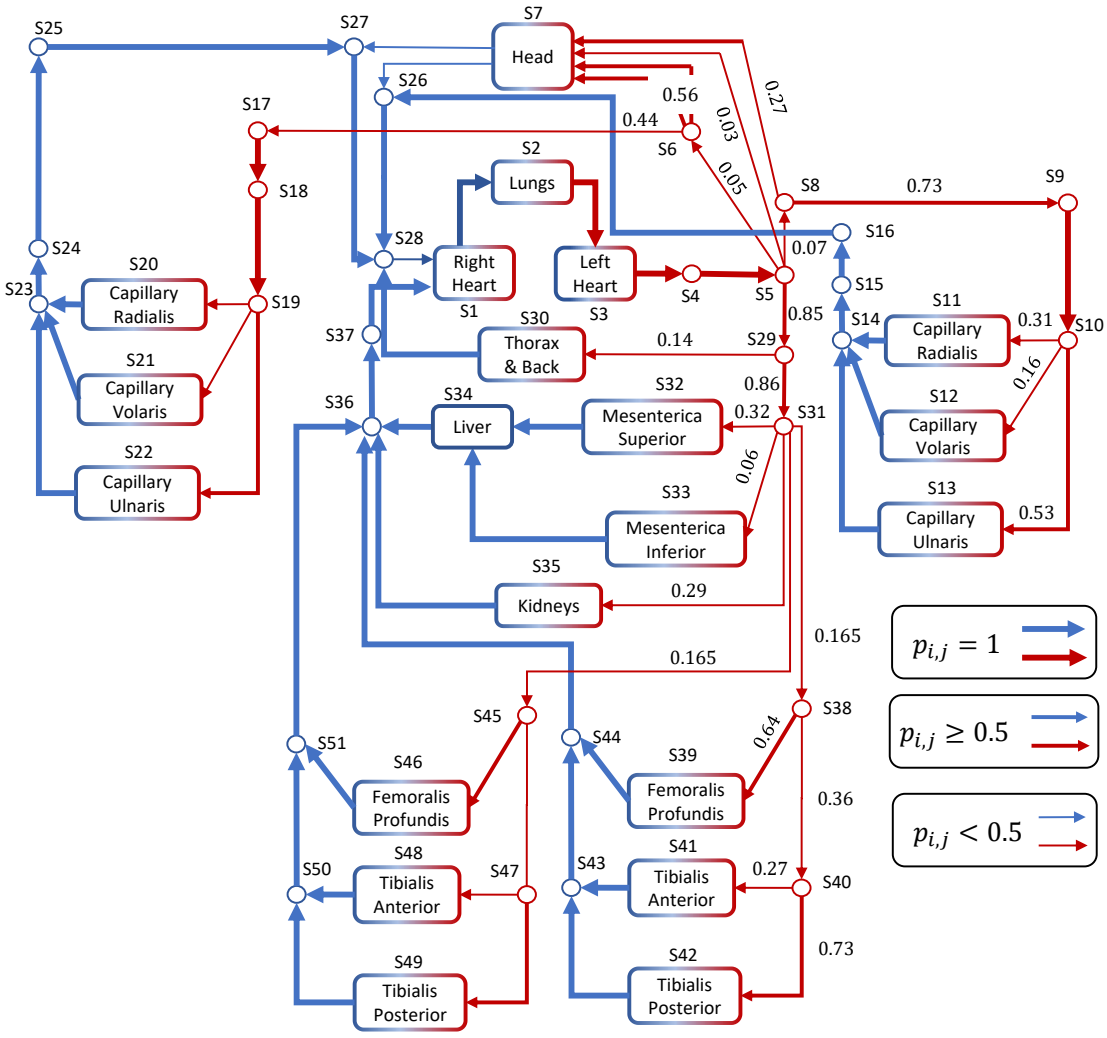

Figure 14: Transition probabilities represented by the width of the edges for $f_{\text{heart}} = 75\,\text{beats/min}$.

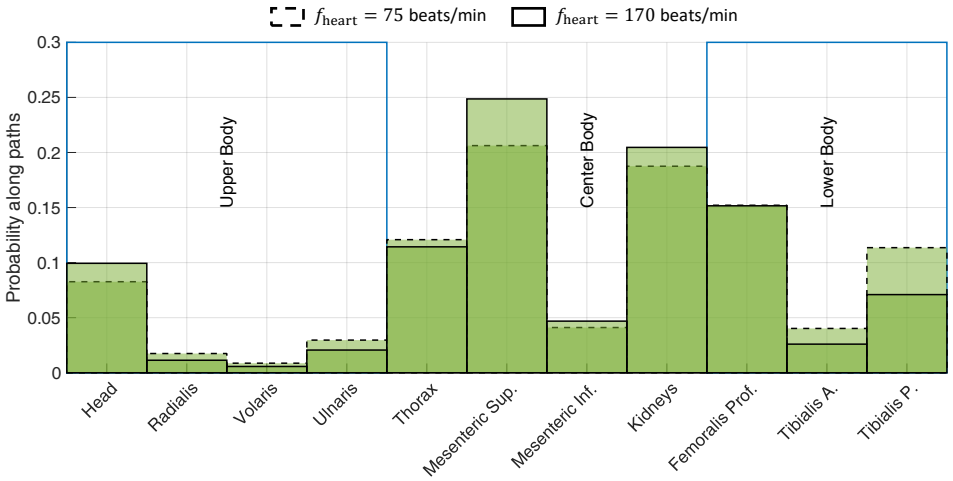

Figure 15: Probability for nanosensors to travel along different paths in the HCS. Bars depict when the body is at rest $f_{\text{heart}} = 75\,\text{beats/min}$ and when doing sports $f_{\text{heart}} = 170\,\text{beats/min}$.

We also illustrate the dynamics of nanosensors when evaluating their probability to follow a path in the HCS. We analyze the probability that a nanosensor travels along different paths as closed loops in the human body. For instance, traveling to the head is along the closed loop S1 to S5, S6 or S8 to S7, and S26 or S27 to S28. We compute

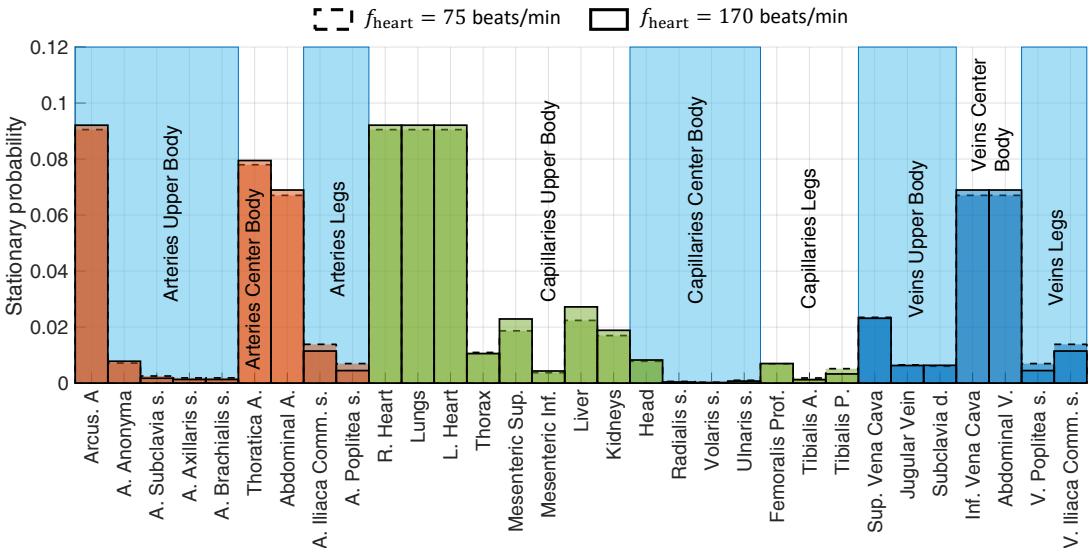

Figure 16: Distribution of nanosensors in the HCS when the body is at rest $f_{\text{heart}} = 75\,\text{beats/min}$ and when doing sports $f_{\text{heart}} = 170\,\text{beats/min}$.

this probability by multiplying and adding the transition probabilities accordingly along this path.

Fig. 15 illustrates the probabilities along the different paths for the two activities. Some paths are more probable than others in the two regimes. For instance, traveling through the loops to the head, Mesenterica Superior, or kidneys results in higher probability when doing sport and the others when resting. Based on these results, the path of the nanosensors will be highly dependent on human activity for most of the body's loops.

Fig. 16 shows the results for the stationary distribution of nanosensors in the vessels. The bars' length indicates the probability of locating a given nanosensor along with the vessel's segments. This figure exhibits a high dependency on human activity. In the sports regime, the concentration of nanosensors will increase in the main vessel segments as arteries, veins in the center body and the legs, and also at most capillaries.

This figure also shows that the largest probability is obtained at the Arcus and Thoracic Aorta, the heart, the Lungs, and the Superior Vena Cava with the two activities. In this case, the probability is around 0.1 which is close to the probability derived in our previous work in [11, Fig. 9]. However, in contrast to our previous work, the Superior Vena Cava exhibits a larger probability than the Inferior Vena Cava. This is a consequence of the inclusion of the two arms and the connection of the Thorax capillaries to the Superior Vena Cava. According to these bars, the less probability to find a nanosensor is given in the Mesenteric Inferior and the capillaries in the arms and legs, also for the two activities regime.

6. Conclusion

This work underlines a practical methodology to predict the concentration of nanosensors traveling in the blood flow and describes their dynamics as a stochastic process. Relying on the Markov model representation of the human circulatory system (HCS), our methodology employs a low-complex electric circuit to evaluate the transition probabilities. In the limit, our Markov model formulation allows us to compute the nanosensor distribution along the vessel segments effectively. Besides, the mobility dynamics of nanosensors can be described by their probability of traveling along the various loops in the body. In our new model, the electric circuit design allows a flexible analysis of the heart frequency, thereby allowing further studies of the impact of human activity, i.e., different heart rates, on the concentration levels of nanosensors in the HCS. This model intends to assist larger designs where knowledge about the expected location of nanosensors becomes critical to assess their actuation and sensing capabilities. In future work, we plan to extend this methodology to evaluate particular individuals. Although the current design is based on a prototype subject, it can be adjusted to fit specific vessel parameters.

Acknowledgment

We want to thank Dr. Bettina Krueger for the very helpful discussion about the physiological parameters of the HCS to validate our electrical circuit model. The reported research was supported by the project NaBoCom, funded by the German Research Foundation (DFG) under grant DR 639/21-2 as well as by the project IoBNT, funded by the Federal Ministry of Education and Research (BMBF, Germany) under grant 16KIS1986K.

References

[1] I. F. Akyildiz, M. Pierobon, S. Balasubramaniam, Moving forward with molecular communication: from theory to human health applications [point of view], Proceedings of the IEEE 107 (2019) 858–865. doi:10.1109/jproc.2019.2913890.

[2] T. Nakano, M. J. Moore, F. Wei, A. V. Vasilakos, J. Shuai, Molecular Communication and Networking: Opportunities and Challenges, IEEE Transactions on NanoBioscience 11 (2012) 135–148. doi:10.1109/TNB.2012.2191570.

[3] U. A. K. Chude-Okonkwo, R. Malekian, B. T. Maharaj, A. V. Vasilakos, Molecular Communication and Nanonetwork for Targeted Drug Delivery: A Survey, IEEE Communications Surveys & Tutorials 19 (2017) 3046–3096. doi:10.1109/comst.2017.2705740.

[4] F. Dressler, S. Fischer, Connecting In-Body Nano Communication with Body Area Networks: Challenges and Opportunities of the Internet of Nano Things, Elsevier Nano Communication Networks 6 (2015) 29–38. doi:10.1016/j.nancom.2015.01.006.

[5] F. Lemic, S. Abadal, A. Stevanovic, E. Alarcón, J. Famaey, Toward location-aware in-body terahertz nanonetworks with energy harvesting, in: 9th ACM International Conference on Nanoscale Computing and Communication (NANOCOM 2022), ACM, Barcelona, Spain, 2022. doi:10.1145/3558583.3558813.

[6] J. Simonjan, B. D. Unluturk, I. F. Akyildiz, In-body Bionanosensor Localization for Anomaly Detection via Inertial Positioning and THz Backscattering Communication, IEEE Transactions on NanoBioscience 21 (2022) 216–225. doi:10.1109/tnb.2021.3123972.

[7] L. Zhou, G. Han, L. Liu, Pulse-Based Distance Accumulation Localization Algorithm for Wireless Nanosensor Networks, IEEE Access 5 (2017) 14380–14390. doi:10.1109/access.2017.2732351.

[8] F. Büther, I. Traupe, S. Ebers, Hop Count Routing: A Routing Algorithm for Resource Constrained, Identity-Free Medical Nanonetworks, in: 5th ACM International Conference on Nanoscale Computing and Communication (NANOCOM 2018), ACM, Reykjavík, Iceland, 2018. doi:10.1145/3233188.3233193.

[9] J. Torres Gómez, A. Kuestner, K. Pitke, J. Simonjan, B. D. Unluturk, F. Dressler, A Machine Learning Approach for Abnormality Detection in Blood Vessels via Mobile Nanosensors, in: 19th ACM Conference on Embedded Networked Sensor Systems (SenSys 2021), 2nd ACM International Workshop on Nanoscale Computing, Communication, and Applications (NanoCoCoA 2021), ACM, Coimbra, Portugal, 2021, pp. 596–602. doi:10.1145/3485730.3494037.

[10] R. Mosayebi, A. Ahmadzadeh, W. Wicke, V. Jamali, R. Schober, M. Nasiri-Kenari, Early Cancer Detection in Blood Vessels Using Mobile Nanosensors, IEEE Transactions on NanoBioscience 18 (2019) 103–116. doi:10.1109/tnb.2018.2885463.

[11] J. Torres Gómez, R. Wendt, A. Kuestner, K. Pitke, L. Stratmann, F. Dressler, Markov Model for the Flow of Nanobots in the Human Circulatory System, in: 8th ACM International Conference on Nanoscale Computing and Communication (NANOCOM 2021), ACM, Virtual Conference, 2021, pp. 5:1–5:7. doi:10.1145/3477206.3477477.

[12] J. Torres Gómez, J. L. González Rios, F. Dressler, Nanosensor Location in the Human Circulatory System based on Electric Circuit Representation of Vessels, in: 9th ACM International Conference on Nanoscale Computing and Communication (NANOCOM 2022), ACM, Barcelona, Spain, 2022, pp. 1–7. doi:10.1145/3558583.3558818.

[13] A. Noordergraaf, P. D. Verdouw, H. B. Boom, The use of an analog computer in a circulation model, Progress in Cardiovascular Diseases 5 (1963) 419–439. doi:10.1016/s0033-0620(63)80009-2.

[14] N. Westerhof, F. Bosman, C. J. D. Vries, A. Noordergraaf, Analog studies of the human systemic arterial tree, Journal of Biomechanics 2 (1969) 121–143. doi:10.1016/0021-9290(69)90024-4.

[15] V. C. Rideout, Mathematical and Computer Modeling of Physiological Systems, Prentice Hall, Upper Saddle River, NJ, 1991.

[16] F. Lemic, S. Abadal, C. Han, J. M. Marquez-Barja, E. Alarcón, J. Famaey, Localization in power-constrained Terahertz-operating software-defined metamaterials, Elsevier Nano Communication Networks 30 (2021) 100365. doi:10.1016/j.nancom.2021.100365.

[17] E. N. Slottke, Inductively Coupled Microsensor Networks: Relay Enabled Cooperative Communication and Localization, Phd thesis, Dep. of Inform.Technol. Electrical Eng., ETH Zürich, 2016. doi:10.3929/ETHZ-A-010860000.

[18] M. Stelzner, I. Traupe, FCNN: Location Awareness Based on a Lightweight Hop Count Routing Body Coordinates Concept, in: 6th ACM International Conference on Nanoscale Computing and Communication (NANOCOM 2019), ACM, Dublin, Ireland, 2019. doi:10.1145/3345312.3345493.

[19] A. Tsioliaridou, C. Liaskos, E. Dedu, S. Ioannidis, Stateless Linear-path Routing for 3D Nanonetworks, in: 3rd ACM International Conference on Nanoscale Computing and Communication (NANOCOM 2016), ACM, New York City, NY, 2016. doi:10.1145/2967446.2967451.

[20] J. Torres Gómez, J. L. González Rios, F. Dressler, Digital Simulator of the Human Arteries, in: European Wireless (EW 2022), VDE, Dresden, Germany, 2022.

[21] R. Gul, Mathematical Modeling and Sensitivity Analysis of Lumped-Parameter Model of the Human Cardiovascular System, Phd thesis, Freien Universität Berlin, 2016.

[22] L. Formaggia, A. Quarteroni, A. Veneziani, The circulatory system: from case studies to mathematical modeling, in: A. Quarteroni, L. Formaggia, A. Veneziani (Eds.), Complex Systems in Biomedicine, Springer Milan, Milano, Italy, 2006, pp. 243–287. doi:10.1007/88-470-0396-2_7.

[23] Y. Shi, P. Lawford, R. Hose, Review of Zero-D and 1-D Models of Blood Flow in the Cardiovascular System, BioMedical Engineering OnLine 10 (2011) 33. doi:10.1186/1475-925x-10-33.

[24] M. F. Snyder, V. C. Rideout, Computer Simulation Studies of the Venous Circulation, IEEE Transactions on Biomedical Engineering BME-16 (1969) 325–334. doi:10.1109/tbme.1969.4502663.

[25] A. C. Guyton, M. E. Hall, Guyton and Hall Textbook of Medical Physiology, 14 ed., Elsevier, 2015.

[26] A. B. Carlson, P. B. Crilly, J. C. Rutledge, Communication Systems: An Introduction to Signals and Noise in Electrical Communication, 4 ed., McGraw-Hill, 2002.

[27] W. Hayt, J. Kemmerly, J. Phillips, S. Durbin, Engineering Circuit Analysis, 9 ed., McGraw-Hill Education, New York City, NY, 2019.

[28] J. L. González Rios, J. Torres Gómez, R. Kumar Sharma, F. Dressler, M. J. Fernández-Getino García, Wideband OFDM-based Communications in Bus Topology as a Key Enabler for Industry 4.0 Networks, IEEE Access 9 (2021) 114167–114178. doi:10.1109/ACCESS.2021.3104741.

[29] C. Gatsonis, J. S. Hodges, R. E. Kaas, N. D. Singpurwalla, Case Studies in Bayesian Statistics, volume II, Springer, 2012.

[30] S. L. Kalpazidou, Genesis of Markov Chains by Circuits: The Circuit Chains, in: B. Rozovskii (Ed.), Cycle Representations of Markov Processes, volume 28 of *Springer*, 2 ed., Springer, 2006, pp. 17–28.